Peer reviewed version

University of Bristol - Explore Bristol Research
General rights

NEAR-FAULT ACCELERATION-PULSES AND NON-ACCELERATION-PULSES: EFFECTS ON THE INELASTIC DISPLACEMENT RATIO

Zhiwang Chang[1], Flavia De Luca[2], and Katsuichiro Goda[3]

[1]School of Civil Engineering, Southwest Jiaotong University, Chengdu 610031, China

[2]Department of Civil Engineering, University of Bristol, Bristol BS81TR, UK

[3]Departments of Earth Sciences and Statistical and Actuarial Sciences, Western University, London N6A5B7, Canada

Summary

Near-fault ground motions can impose particularly high seismic demands on the structures due to the pulses that are typically observed in the velocity time-histories. The velocity-pulses can be further categorized into either a distinct acceleration-pulse (*acc-pulse*) or a succession of high-frequency, one-sided acceleration spikes (*non-acc-pulse*). The different characteristics of velocity-pulses imply different frequency-content of the ground motions, potentially causing different seismic effects on the structures. This study aims to investigate the characteristics of the two types of velocity-pulses and their impacts on the inelastic displacement ratio (C_R) of single-degree-of-freedom systems. First, a new method that enables an automated classification of velocity-pulses is used to compile a ground motion dataset which consists of 74 *acc-pulses* and 45 *non-acc-pulses*. Several intensity measures characterizing different seismological features are then compared using the two groups of records. Finally, the influences of *acc-pulses* and *non-acc-pulses* on the C_R spectra are studied; the effects of pulse period and hysteretic behavior are also considered. Results indicate that the characteristics of the two types of velocity-pulses differ significantly, resulting in clearly distinct C_R spectral properties between *acc-pulses* and *non-acc-pulses*. Interestingly, mixing *acc-pulses* and *non-acc-pulses* can lead to local 'bumps' that were found in the C_R spectral shape by previous studies. The findings of this study highlight the importance of distinguishing velocity-pulses of different types when selecting near-fault ground motions for assessing the nonlinear dynamic response of structures.

KEYWORDS

near-fault ground motion, acceleration-pulse, velocity-pulse, Bouc-Wen model, inelastic displacement ratio

1. INTRODUCTION

Seismic behavior and consequent damage of a structure can be strongly influenced by its location relative to the ruptured earthquake fault. When the structure is located within an area close to the seismic fault, e.g., within 30 km,[1] particularly high seismic demands are usually imposed. Specifically, the seismic damage within a near-fault region is often caused during a few cycles of severe inelastic deformation that coincides with large amplitude velocity-pulses in the ground motions. In contrast, the damage resulting from far-field ground motions is typically caused by the repeated cycles of inelastic deformation that accumulates in the structural components.[2] Previous studies comfirmed that key features of the velocity-pulse, e.g., amplitude, predominant period and the pulse shape, play important roles in affecting the structural response, and are primarily affected by the earthquake source characteristics, location of the recording station relative to the fault rupture as well as the site effects.[3]

During the past two decades, near-fault pulse-like ground motions have been extensively studied by the seismology and earthquake engineering community. From the seismological perspective, numerous studies have been carried out by: using analytical models to characterize the velocity-pulses,[4-6] accounting for the pulse effects in seismic hazard analysis,[7-8] simulating pulse-like ground motions using stochastic approaches,[9-10] and classifying velocity-pulses through automated algorithms.[11-13] From the engineering perspective, the effects of pulse-like ground motions on various structures have been investigated, including: idealized single (or multi)-degree-of-freedom (SDOF) systems,[14-15] seismically base-isolated structures,[16-17] bridge structures,[18-19] and some other special buildings or elements.[20-23] A common finding in the above studies is that the effects of pulse-like ground motions significantly depend on the relative characteristics of the velocity-pulse and the dynamic properties of the structure. Specifically, when the fundamental vibration period (T) of the structure is equal or close to the period of the predominant velocity-pulse, larger seismic demands are usually required.

In the above studies, further classifications of the near-fault ground motions, beyond the characterization of velocity-pulses, are rarely discussed and largely overlooked in the literature. In fact, the velocity-pulse can be further categorized into either a distinct acceleration pulse (*acc-pulse*) or a succession of high-frequency, one-sided acceleration spikes (*non-acc-pulse*). For illustration, two example ground motions, recorded during the 1987 Whittier Narrows-01 earthquake and the 1999 Chi-Chi earthquake, are shown in Figure 1. Dominant pulses can be identified by visually inspecting velocity time-histories of the two records. Yet after examining their acceleration time-histories more carefully, the two dominant velocity-pulses are observed to contain significantly different frequency content. Specifically, in Figure 1a, the velocity-pulse is an integral of a distinct low-frequency *acc-pulse*; while in Figure 1b the velocity-pulse is an integral of a series of high-frequency, one-sided splikes. The velocity-pulses having different frequency content can cause different impacts on the structures. An *acc-pulse*, such as the Whittier Narrows expample in Figure 1a, is more damaging to structures with short-to-moderate periods (T=1.5-2.5s), while a *non-acc-pulse*, such as the Chi-Chi example in Figure 1b, has significant impacts on long-period structures (T>4s).[24-25]

Despite the potential significance of different seismic demands resulting from the two types of velocty-pulses, investigations on this topic are limited, except for a few pioneer studies.[24-25] No systematic statistical analyses have been carried out. In this regard, a new algorithm[26] for automatically classifying *acc-pulses* and *non-acc-pulses* can be implemented to perform a comparative study to reveal how the velocity-pulses of different characteristics may affect the inelastic response of structures. Following the compilation of the two groups of velocity-pulses, the characteristics of *acc-pulses* and *non-acc-pulses* are studied, and the effects on the inelastic displacement ratio (C_R) are systematically investigated. In Section 2, the algorithm for identifying *acc-pulses* and *non-acc-pulses* is briefly explained, and two suites of *acc-pulse* and *non-acc-pulse* ground motions are compiled from the Next Generation Attenuation West 2 database (or NGA West 2).[27] In Section 3, intensity measures representing various ground motion characteristics are compared with respect to the two groups of velocity-pulses. Finally, in Section 4, the C_R values are obtained by means of the Bouc-Wen model,[28] and the C_R spectra are compared between *acc-pulses* and *non-acc-pulses*. The effects of pulse period (T_p) and hysteretic behavior of the Bouc-Wen system on the C_R spectra are also taken into account. In addition, the C_R spectra derived from the two types of velocity-pulses are compared with existing C_R prediction models. One of the insteresting findings in this study is that mixing the *acc-pulses* and *non-acc-pulses* can lead to local 'bumps' in the C_R spectral shape. The 'bumps' were also noted by previous studies,[29-30] but the reason of how these 'bumps' are produced was not revealed. To the best of our knowledge, authough there are plenty of studies contributing to the subject of C_R,[29-35] no efforts have been devoted to analyzing the differences in terms of C_R that are introduced by velocity-pulses having different characteristics. The pronounced differences in C_R that are observed in this study highlight the importance of distinguishing *acc-pulses* and *non-acc-pulses* when selecting near-fault ground motions for carrying out nonlinear dynamic analysis.

2.   CLASSIFICATION ALGORITHM FOR ACC-PULSES AND NON-ACC-PULSES

2.1   Pulse classification algorithm

For classifying *acc-pulses* and *non-acc-pulses*, two main steps are required, see Figure 2. More details about this algorithm can be found in Chang et al.[26] The main procedures for performing such a classification are as follows:

1. In the first step, for a *velocity* time-history shown in Figure 2a, the wavelet packet transform (WPT) is used to remove the high-frequency content. This can be achieved by keeping the top wavelet packet coeffecints (WPCs) that account for 70% of the total WPCs, while setting all remaining WPCs to zeroes. Using the inverse-WPT, the main velocity-pulse can be extracted. With respect to the extracted velocity-pulse data, the pulse-starting and -ending time instants (t_s and t_e) can be determined according to the peak-point-method (PPM),[12] see Figure 2b. The time interval between t_s and t_e can be used for deriving T_p.
2. With respect to the original velocity time-history, calculate the relative cumulative squared velocities (CSV) as well as the relative energy of the velocity-pulse (EVP), see Figure 2c. EVP is mathematically defined as follows:

$$\text{EVP} = \text{CSV}(t_e)\text{-CSV}(t_s) = \frac{\int_0^{t_e} v^2(\tau)d\tau}{\int_0^D v^2(\tau)d\tau} - \frac{\int_0^{t_s} v^2(\tau)d\tau}{\int_0^D v^2(\tau)d\tau}, \tag{1}$$

where D indicates the total duration of the ground motion; $v(t)$ represents the velocity time series. When the EVP is larger than 0.35, significant velocity-pulse features can be detected.

3. For ground motions containing velocity-pulses, t_s and t_e are retrieved in the original *acceleration* time-history, and a local acceleration time-history is then extracted, see Figures 2d and 2e.

4. Using the extracted acceleration time-history, all zero-crossings are identified. The cumulative squared accelerations (CSA) as well as the energy of the *acc-pulse* (EAP) between every two adjacent zero-crossings are calculated. Here EAP is expressed as:

$$EAP = CSA(t_2)\text{-}CSA(t_1) = \frac{\int_{t_s}^{t_2} a^2(\tau)\, d\tau}{\int_{t_s}^{t_e} a^2(\tau)\, d\tau} - \frac{\int_{t_s}^{t_1} a^2(\tau)\, d\tau}{\int_{t_s}^{t_e} a^2(\tau)\, d\tau} , \qquad (2)$$

where t_1 and t_2 are the time-starting and -ending time instants of the half-cycle pulse; and $a(t)$ indicates the acceleration time series of the extracted ground motion. The maximum EAP is used as the indicator for classifying *acc-pulses*, see Figure 2f. When the EAP is smaller than 0.25, the record is classified as *non-acc-pulse*; when it is larger than 0.50, the record is classified as *acc-pulse*. The records with EAP falling between 0.25 and 0.50 are not classified as either *non-acc-pulses* or *acc-pulses*, and are not used in this study (i.e., they require further examinations).

In this study, special attention is given to velocity-pulses that are related to the forward-directivity effects.[3] The method proposed in Zhai et al.[12] is here adopted to detect early-arriving pulses that are more likely to be caused by forward-directivity. However, it should be noted that the most reliable way of selecting forward-directivity pulses is by examining the source-to-site geometry of the recording station with respect to the fault rupture, as done by Shahi and Baker.[36] This latter method is applicable but can be very time-consuming when dealing with tens of hundreds of ground motions on a case-by-case basis.[37] Moreover, no record-rotations to the fault-normal and -parellel directions are applied herein, noting that such operations do not always lead to maximum responses over all angles.[38]

2.2 Application to the 1999 Chi-Chi earthquake records

Forward-directivity effects can occur when two main conditions are satisfied: the rupture front propagates towards a near-fault site, and the direction of rupture on the fault is aligned with the site.[3] Although the above algorithm for classifying pulse-like ground motions does not involve any seismological parameters (e.g., site location relative to the rupture and the distance between the rupture and the site), results of the classified records can be compared with empirical observations.

To this aim, the 1999 Chi-Chi earthquake ground motion data are considered and shown in Figure 3. The earthquake occurred in the middle of the island at 23.78 N˚ and 120.81E˚, and it was associated with the Chelungpu fault with a hypocenter depth at around 7 km. According to the earthquake rupture model by Zeng and Chen,[39] the along-strike length and along-dip width were 96 km and 40 km, respectively. The surface projection of the earthquake rupture model is represented by a red dashed rectangle. The fault rupture of this event was mainly an east-dipping thrust with a significant left-lateral strike-slip component at the northern section. The strike angle of the earthquake was at 5˚, with the average dip and rake angles at 40˚ and 55˚, respectively. In Figure 3a, all ground motions and those records with peak ground velocity (PGV)>30 cm/s are indicated; while in Figure 3b all velocity-pulses identified using the algorithm in Section 2.1 are labelled. By comparing Figure 3b with Figure 7a in Zeng and Chen,[39] it can be observed that the stations where velocity-pulses were recorded are situated on areas where the ground deformed towards the recording sites. In other words, the velocity-pulses are generally observed at locations near the fault where the rupture front propagated towards the recording sites. The studies in Wu et al.[40] and Spudich et al.[41] can further support this observation, which is broadly in agreement with the above conditions for causing forward-directivity effects.

Among all 1199 ground motions (each containing 2 components), 208 components have PGV values of larger than 30 cm/s, of which 73 are identified as having significant velocity-pulse features. These velocity-pulses are then further analyzed to examine if they possess *acc-pulse* or *non-acc-pulse* features. The results are presented in Figures 3c and 3d, respectively. Out of the 73 velocity-pulses, 15, 28 and 30 are classified as *acc-pulses*, *non-acc-pulses* and ambiguous, respectively. Although many of the velocity-pulses were recorded at reltively short distances, *non-acc-*

pulses can occur at long source-to-site distances more often than *acc-pulses*; see dashed ellipses in Figures 3c and 3d. This observation may only apply to this particular case of the Chi-Chi earthquake, since it was a well-recorded event with a significant number of pulse-like records.

3. SEISMOLOGICAL FEATURES OF ACC-PULSES AND NON-ACC-PULSES

To systematically analyze the different characteristics of *acc-pulses* and *non-acc-pulses*, the algorithm outlined in Section 2.1 is applied to an expanded ground motion dataset. Specifically, the dataset consists of 320 ground motions each with two horizontal components, which are the same as those used in Chang et al.[26] They were recorded in earthquake events with moment magnitude (M_w) ≥ 5.5 and at least one of the two horizontal components has PGV value of larger than 30 cm/s. After applying the pulse identification algorithm, 74 *acc-pulses* and 45 *non-acc-pulses* are identified (see the Appendix for further information). It should be noted that these 119 components are all identified as early-arriving pulses and can be considered as potentially caused by the forward-directivity effects.

The seismological characteristics of all ground motion components are illustrated in Figure 4. Figure 4a displays the distribution of M_w versus R_{rup} (the closest distance from the recording site to the ruptured fault area). The majority of *acc-pulses* (59 out of 74) are recorded in earthquake events with M_w no larger than 7; while *non-acc-pulses* are more likely to be observed in larger M_w events (30 out of 45). In addition, only 6 of the 119 velocity-pulses are collected from stations with R_{rup} larger than 30km, meaning that the majority of velocity-pulses can be seen as recorded in near-fault regions. Figure 4b presents the relationship between M_w and V_{s30} (shear-wave velocity averaged in the top 30m of soil). 114 out of the 119 motions are observed at sites with V_{s30} ranging from 180 to 760 m/s, corresponding to the stiff site classes of C and D in terms of the NEHRP program's site classification. Figures 4c and 4d show the distribution of peak ground acceleration (PGA) and PGV with M_w. Although it is more likely to be observed in larger M_w events, the majority of *non-acc-pulses* tends to have smaller PGAs; 37 of the 45 *non-acc-pulses* (82%) have PGA values less than 0.5g. Whereas the *acc-pulses* can possess larger PGA values; 23 out of the 74 *acc-pulses* (31%) have PGA values larger than 0.5g, comparing with 8 out of 45 (18%) for *non-acc-pulses*. Based on Figure 4d, PGVs for most of the *non-acc-pulses* (37 of 45) fall into a range between 30 and 60 cm/s; while of all *acc-pulses*, there are 32 components having PGVs larger than 60 cm/s. That is, in the large PGV range (e.g., >60 cm/s), *acc-pulses* occur more frequently than *non-acc-pulses*.

Figures 5a and 5b present the relation between M_w and the significant duration.[42] The 5-95% significant duration (D_{5-95}) is calculated as the interval between the times at which 5% and 95% of the Arias intensity of the ground motion are reached, representing the time duration over which 90% of the energy is accumulated. The 5-75% significant duration (D_{5-75}) is the time interval from 5% to 75% of Arias intensity and represents 70% of total energy. In general there is a positive correlation between M_w and D_{5-95} (D_{5-75}), i.e., the significant duration increases with M_w. *Acc-pulses* tend to have shorter significant durations; this is especially true when D_{5-75} is considered, see Figure 5b. 48 of the 74 *acc-pulses* have D_{5-75} *smaller* than 5s, while 40 of the 45 *non-acc-pulses* have D_{5-75} *larger* than 5s. This evidence indicates that most of the energy for *acc-pulses* is concentrated within a shorter duration, whereas the energy for *non-acc-pulses* is distributed over a longer duration.

Another relevant parameter for pulse-like motions is T_p. Currently, there is no unique way for calculating T_p. One of the frequently-used methods is based on the velocity-response-spectrum (hereafter abbreviated as the S_v method). It chooses the period at which the peak of the spectrum is achieved.[43] In Figure 5c, T_p calculated using the PPM is compared with the S_v-based T_p. It is seen that T_p values obtained by the two methods are close; and the correlation coefficient for all records reaches 0.85. By further examining the two groups of velocity-pulses, T_p values calculated by PPM for the *acc-pulses* are found to be much closer to the S_v-based T_p. For this case, the correlation coefficient attains 0.92, in contrast to 0.69 for *non-acc-pulses*; this is particularly true for velocity-pulses with T_p smaller than 3s (see shaded area). The discrepancy in T_p estimation shown in Figure 5c can be explained through Figure 6, in which the top panels are for a typical *acc-pulse* while the bottom panels for a *non-acc-pulse*. The T_p for the *acc-pulse* in Figure 6a is 0.77s by the PPM and 0.8s by S_v. While the T_p for the *non-acc-pulse* in Figure 6c is 5.5s by the PPM and 1.4s by S_v. Apparently, the T_p of 5.5s is much closer to the dominant period of the velocity-pulse shown in Figure 6c. Using Baker's algorithm,[11] the dominant velocity-pulses are extracted, and the *acc-pulses* can be obtained by time-differentiation of the velocity-pulse time-histories. It is clearly seen from the acceleration time-history in Figure 6a that the *acc-pulse* is directly related to the velocity-pulse. Whereas for the *non-acc-pulse* in Figure 6c, there are two primary sources affecting the velocity-pulse: the first is the one extracted using Baker's algorithm and the second is the *acc-pulse* confined in the dashed ellipse. S_v for the *acc-pulse* just has one peak (at 0.8s, see Figure 6b), whereas S_v

for the *non-acc-pulse* has two local peaks (at 1.4s and 6.1s, see Figure 6d). This explains the reason why T_p values calculated using the PPM are much closer to the S_v-based T_p for *acc-pulses* than for *non-acc-pulses*. Figure 5d shows that there is a positive correlation between M_w and T_p, which is in agreement with early findings.[4] Based on the ground motion dataset used in this study, *acc-pulses* appear to have smaller T_p compared with *non-acc-pulses* having larger T_p; 65 of the 74 *acc-pulses* have T_p <3.0s, while 40 of the 45 *non-acc-pulses* have T_p >3.0s. This means that *acc-pulses* and *non-acc-pulses* may have distinct impacts on structures having different dynamic properties. *Acc-pulses* are more likely to affect short-period structures, while *non-acc-pulses* are more damaging for long-period structures. This conjecture is consistent with previous studies.[24-25]

Figure 7 shows the distribution between the record number and the usable period (T') for the *acc-pulses* and *non-acc-pulses*. According to the NGA West 2 database, the usable period limit can be defined by the frequency above which the spectra from high-pass filtered data are relatively unaffected by the filter. It is shown that for the *non-acc-pulses*, there is almost no reduction in the record number over the displayed period range, while a significant decrease in the *acc-pulse* number can be observed when T'>8.0 s. Following this, it is assumed that the C_R spectra can be calculated up to T=6.0s so that the majority of data for *acc-pulses* and *non-acc-pulses* can be used.

Figure 8 exhibits the comparisons between the 74 *acc-pulses* and the 45 *non-acc-pulses* in terms of the 5%-damped pseudo-spectral-acceleration (PSA). The median, 16th and 84th percentiles of PSA are displayed in Figures 8a and 8b for the *acc-pulses* and *non-acc-pulses*, respectively. The median PSA for *acc-pulses*, *non-acc-pulses* and all records are compared in Figure 8c, from which it is seen that the PSA values for the *acc-pulses* are larger in the period range T<2.5s than those for the *non-acc-pulses*; whereas an opposite trend is observed for T>2.5s. Figure 8d shows the response spectra with T normalized by T_p. The spectral values for *acc-pulses* are particularly larger than those for *non-acc-pulses* around T/T_p=1, meaning that when the vibration period is close to pulse period, *acc-pulses* can cause significantly larger seismic demands than *non-acc-pulses*.

4. INFLUENCE ON THE INELASTIC DISPLACEMENT RATIO

4.1 Bouc-Wen model for representing SDOF systems

The Bouc-Wen model offers a flexible hysteresis representation of the nonlinear behavior of the structural components or systems under cyclic loading; and it can be characterized by twelve parameters, including the shape parameters $\{\alpha, \beta, \gamma, n\}$, degradation parameters $\{\delta_\nu, \delta_\eta\}$ and pinching parameters $\{\zeta_s, q, p, \Psi, \delta_\Psi, \lambda\}$. The equations of motion for SDOF systems can be found in Goda et al.[28] Figure 9 illustrates the general relationships between the ductility demand μ and the normalized restoring force $\alpha\mu + (1-\alpha)\mu_z$ with respect to four Bouc-Wen models that are considered in this study; μ_z is hysteretic ductility demand. The four models include the elastic-perfectly-plastic system (EPP), bilinear system (EPH), degrading system (EPH-d) and the degrading system with pinching effects (EPH-dp). In the following, the default Bouc-Wen parameters are set as those for the EPP. The effects of hysteretic models on the C_R spectra are considered in Section 4.5.

4.2 Effect of R

Under the constant-strength condition, C_R is expressed as the maximum inelastic displacement divided by the maximum elastic displacement of a SDOF system having the same dynamic properties (i.e., mass, damping ratio, and fundamental vibration period). The strength reduction factor R is defined as:

$$R = mS_a/f_y, \tag{3}$$

where m is the structure mass; S_a indicates the elastic PSA at a specific T; and f_y is the yield force. In this study, the C_R spectra are computed for SDOF systems having four R levels: 1.5, 2, 4 and 6.

Figures 10a and 10b illustrate the median C_R spectra for *acc-pulses* and *non-acc-pulses*, respectively. The spectra for the two suites of velocity-pulses are clearly different, although overall all spectra follow a similar exponentially decaying tendency. The spectra in Figure 10a for *acc-pulses* are more similar to existing models,[29] among which the C_R values sharply decrease with T in the short-period range (T<1.0s), and remain constant around unity in the medium- and long-period ranges. In Figure 10b, the C_R spectra for *non-acc-pulses* under low R levels (R=1.5 and 2) are similar

to those for *acc-pulses*; while under high R levels (R=4 and 6), the C_R spectra have amplified bumps in the medium- and long-period ranges (1.0s<T<4.0s). The maximum C_R near the bump reaches up to 1.9 at T=1.5s, in contrast to 1.0 at the same T for *acc-pulses*. This observation is reinforced after calculating the C_R spectral ratios ($C_{R,\ non-acc-pulses}$ / $C_{R,\ acc-pulses}$) of *non-acc-pulses* with respect to *acc-pulses*, as shown in Figure 10c. It is seen that under low R levels (R=1.5 and 2), the spectral ratios are close to unity over almost the whole period range. Whereas under high R levels (R=4 and 6), two completely opposite trends are observed along the period range separated at T=0.6s. In the short-period range (T<0.6s), $C_{R,\ non-acc-pulses}$ / $C_{R,\ acc-pulses}$ is clearly smaller than 1.0, meaning that in this range the *acc-pulses* can have a much larger impact on C_R than the *non-acc-pulses*. While in the range T>0.6s, $C_{R,\ non-acc-pulses}$ / $C_{R,\ acc-pulses}$ is obviously larger than 1.0 till T=4.0s, meaning that the *non-acc-pulses* have a much greater influence on C_R over this range. Noting that for large R values (R=4 and 6) there is a local 'outlier' at the beginning period of T=0.01s, at which $C_{R,\ non-acc-pulses}$ / $C_{R,\ acc-pulses}$ is unexpectedly larger than 1.0. According to Erduran and Kunnath,[44] strength and stiffness are highly correlated, and it is very unlikely to design structures with short vibration periods and large R values. Therefore, we suppose that this local 'outlier' could be reasonably ignored, as it might be unrealistic to construct very stiff structures (e.g., T=0.01s) under high R levels (R=4 and 6).

4.3 Effect of T_p

Pulse period is known as one of the most important parameters in predicting the structural response. Past studies[30-31] showed that presenting the C_R spectra with T normalized by T_p can provide a better ground motion characterization and reduce the record-to-record variability. The normalized C_R spectra for *acc-pulses* and *non-acc-pulses* are then shown in Figures 11a and 11b, respectively. The differences in the C_R spectra for the two types of velocity-pulses largely lie within the short T/T_p range (T/T_p <1.0). The spectra for *acc-pulses* in Figure 11a follow a trend similar to the results shown by Ruiz-Garcia.[29] However, for the *non-acc-pulses* in Figure 11b, the most remarkable features are the local amplification or 'bumps' falling into a range around T/T_p=0.5 that are not consistently observed in Figure 11a under high R levels (R=4 and 6). These bumps were also reported by Ruiz-Garcia,[29] and an analytical equation was derived by Iervolino et al.[30] to better capture this peculiar spectral shape. Although it is argued that their equation can well predict the local bumps, our results can shed more light for the cause of this shape. More specifically, this spectral shape can be attributed to be a consequence of having incorporated both *acc-pulses* and *non-acc-pulses*. Further evidence to support this argument is presented in the next section. Figure 11c displays the C_R spectral ratios of *non-acc-pulses* to *acc-pulses*, which are similar to those in Figure 10c but with T normalized by T_p. It is observed that for T/T_p <0.8, $C_{R,\ non-acc-pulses}$ / $C_{R,\ acc-pulses}$ is consistently smaller than 1.0; the ratios for systems having large R values (R=4 and 6) are smaller than those with small R values (R=1.5 and 2), and it becomes larger as T/T_p increases. The observation of $C_{R,\ non-acc-pulses}$ / $C_{R,\ acc-pulses}$ <1.0 indicates that *acc-pulses* can generally impose much larger seismic demands than *non-acc-pulses* for a structure with fundamental vibration period smaller than the pulse period. When T/T_p >0.8, $C_{R,\ non-acc-pulses}$ / $C_{R,\ acc-pulses}$ for systems of small R values (R=1.5 and 2) remains almost unvaried and close to 1.0; while for systems having large R values (R=4 and 6), $C_{R,\ non-acc-pulses}$ / $C_{R,\ acc-pulses}$ can be larger than 1.0 up to T/T_p =1.5, after which it begins falling below 1.0 again. Nevertheless, considering that the absolute values of C_R for T/T_p >0.8 are not significantly larger and close to 1.0 (see Figures 11a and 11b), it is supposed that for systems of large R values (R=4 and 6) this fluctuating trend of $C_{R,\ non-acc-pulses}$ / $C_{R,\ acc-pulses}$ can be negligible when T/T_p >0.8. The non-significance of this fluctuation indicates that there can be no big difference in C_R when considering medium- to long-period systems under high R levels (R=4 and 6).

4.4 Comparison with existing models and local 'bumps' in C_R spectra

The effects of forward-directivity velocity-pulses on C_R were investigated by Ruiz-Garcia,[29] without distinguishing *acc-pulses* and *non-acc-pulses*. The C_R equation developed in that study is as follows:

$$C_R = 1 + (R-1)\left[\frac{1}{\theta_1\left(T/T_g\right)^2}\right] + \theta_2\left(T_g/T\right)\exp\left[\theta_3 \ln\left(T/T_g - 0.08\right)^2\right] \tag{4}$$

where T_g is the predominant period of ground motion and is equal to T_p determined by S_v. Because of the strong correlation between T_p and T_g, as seen in Figure 5d, in the following T/T_p is used in lieu of T/T_g. $\theta_1 \sim \theta_3$ are constants

that depend on the level of R. Comparisons of the C_R spectra for R=2, 4 and 6 are shown in Figure 12; the C_R spectra for R=1.5 is not provided since relevant $\theta_1 \sim \theta_3$ are not available in Ruiz-Garcia.[29] Overall the prediction model is capable of fitting the C_R spectra for *acc-pulses*, especially when T/T_p<1.0. However the model cannot capture the spectra for *non-acc-pulses* when T/T_p<0.5 because of the presence of local bumps; noting that the bumps for R=2 are not as significant as those for R=4 and 6. When T/T_p>1.0, it is observed that for R=2, the model is good at fitting the C_R spectra for both *acc-pulses* and *non-acc-pulses*; yet it can slightly overestimate C_R for R=4 and 6. Iervolino et al.[30] proposed an analytical equation to characterize the bumps; since their underlying SDOF system is different from the default model in the present study (bilinear with 3% post-yield stiffness *versus* the EPP used herein), a direct comparison with their prediction is not further pursued here. However, it is desirable to demonstrate that this special shape of local bumps is a result of having mixed different proportions of *acc-pulses* and *non-acc-pulses*. Figure 13 displays the C_R spectra for a mixture of the two types of velocity-pulses, in which the number of *acc-pulses* is varied while keeping unvaried the number of *non-acc-pulses*. Specifically, Figures 13a, 13b and 13c represent three particular record-grouping cases among which the number of *acc-pulses* is more than (74 *versus* 45), equal to (45 *versus* 45) and less than (20 *versus* 45) that of *non-acc-pulses*, respectively. Figure 13 together with Figures 11a (in which all records are *acc-pulses*) and 11b (in which all records are *non-acc-pulses*) clearly show that as the proportion of the two groups of records changes, the local bumps are progressively becoming more and more evident, especially for systems under high R levels (R =4 and 6). Additionally, it is found that these bumps can be seen for *non-acc-pulses* when other hysteretic models are considered, and the bumps can get more pronounced as the hysteretic model changes from EPP to EPH-dp, see Figure 14. However, similar bumps are not found for *acc-pulses*; these are not displayed for the sake of brevity.

4.5   Effect of hysteretic models

To examine the effect of hysteretic models on the C_R spectra under *acc-pulses* and *non-acc-pulses*, ratios of the C_R spectra for EPH, EPH-d and EPH-dp systems to the C_R spectra for EPP systems are calculated for each record group and each R level; and the mean ratios are shown in Figure 15. It is observed that for all EPH and EPH-d systems as well as the EPH-dp systems under high R levels (R=4 and 6), the mean ratio becomes smaller as T decreases and as R increases. In the short-period range (T<1.0s), the mean ratio is generally smaller than 1.0, meaning that the C_R spectra for these systems are on average smaller than those for EPP systems. In the medium- to long-period range (T>1.0s), the mean ratio is close to 1.0, meaning that changing the hysteretic models would not significantly alter the C_R spectra, and that the C_R spectral values for these systems can be approximate to those for EPP systems. This observation is also applicable for EPH-dp systems under low R levels (R=1.5 and 2) when T>1.0s, see Figure 15c for *acc-pulses* and Figure 15f for *non-acc-pulses*. However, for EPH-dp systems of small R values (R=1.5 and 2) in short-period ranges (T<1.0s), the mean ratio may have an inverted V-shape. The C_R ratios at the beginning of this short-period range are clearly smaller than 1.0; yet they can then increase up to much larger values (>1.0) at the latter part of this short-period range. This is particularly true for *non-acc-pulses*, in which the largest mean ratio reaches 3.3 for R=1.5 and 2.2 for R=2, see Figure 15f. By carefully comparing the short-period mean ratios for *acc-pulses* and *non-acc-pulses* shown throughout Figure 15, it is found that with respect to a specific short-period SDOF system (T<1.0s), the mean ratios for *non-acc-pulses* are relatively larger than those for *acc-pulses*; and this difference tends to increase as the considered hysteretic model varies from EPH to EPH-dp. Moreover, as R increases, the mean ratios for the two types of velocity-pulses gradually become closer to each other, see Figure 16 for an example SDOF system with T=0.1s.

5.   CONCLUSIONS

Using a new algorithm[26] for classifying *acc-pulses* and *non-acc-pulses*, this study first discussed the characteristics of the two types of velocity-pulses that are considered forward-directivity-related, and then the effects on the inelastic displacement ratio (C_R) were investigated. The main findings are as follows:

1. Taking advantage of the 1999 Chi-Chi earthquake ground motion data, this study illustrated that velocity-pulses can be generally observed at locations near the fault where the rupture front propagates towards the recording sites, which agrees with existing seismological models.
2. Compared with *non-acc-pulses*, *acc-pulses* are more likely to be observed in smaller-magnitude earthquake events, yet tend to have larger PGA and PGV values. The *acc-pulses* have shorter significant durations and smaller pulse periods (T_p), meaning that the energy of *acc-pulses* are more concentrated within a short-duration time interval and larger seismic demands can be expected on short-period structures.

3. The pulse periods for *acc-pulses* are usually associated with visible pulses in the acceleration histories; whereas the pulse periods for *non-acc-pulses* might be influenced by high-frequency oscillatory portion of the ground motion. This explains the reason why pulse periods calculated by the peak-point-method for *acc-pulses* are much closer to those derived from the pseudo-velocity-spectrum.

4. For *acc-pulses* under all considered R values and for *non-acc-pulses* under small R values (R=1.5 and 2), the C_R spectral values sharply decrease with the increase of the vibration period (T) in the short-period range (T<1.0s) and remain constant around unity in the medium- to long-period ranges. For *non-acc-pulses* under large R values (R=4 and 6), the C_R spectra can have bumps in the medium- to long-period ranges (1.0s<T<4.5s).

5. When T is normalized by T_p, the C_R spectra for *acc-pulses* under all interested R values and for *non-acc-pulses* under small R values (R=1.5 and 2) are more approximate to existing models. For *non-acc-pulses* under large R values (R=4 and 6), local bumps are observed around T/T_p=0.5. The bumps are shown to be a result of mixing *acc-pulses* and *non-acc-pulses*, and are mainly induced by the *non-acc-pulses*. The bumps may be consistently found for *non-acc-pulses* when all hysteretic models are considered, and can get more pronounced as the model changes from EPP to EPH-dp.

6. In the short-period range (T<1.0s), the mean $C_{R,\,\text{EPH-dp}} / C_{R,\,\text{EPP}}$ for systems having large R values (R=4 and 6) can exhibit a trend that is different from the mean $C_{R,\,\text{EPH}} / C_{R,\,\text{EPP}}$ and $C_{R,\,\text{EPH-d}} / C_{R,\,\text{EPP}}$ under all R levels. For short-period SDOF systems (T<1.0s), the C_R spectral ratios for *non-acc-pulses* are relatively larger than those for *acc-pulses*. The difference in the C_R ratios tends to get larger as the hysteretic model varies from EPH to EPH-dp, and get smaller as R increases.

The above conclusions demonstrate that there are significant differences in the characteristics of *acc-pulses* and *non-acc-pulses*, and the seismic demands imposed by the two types of velocity-pulses can be quite distinct. The findings highlight the importance of distinguishing velocity-pulses of different characteristics when selecting near-fault ground motions for performing seismic assessments of structures. In the future, more extensive studies are needed to investigate how multi-degree-of-freedom systems may be affected by the two types of velocity-pulses.

ACKNOWLEDGMENTS

REFERENCES

1. Iervolino I, Cornell CA. Probability of occurrence of velocity pulses in near-source ground motions. *Bull Seismol Soc Am*. 2008; 98(5): 2262-2277.
2. Kalkan E, Kunnath SK. Effects of Fling Step and Forward Directivity on Seismic Response of Buildings. *Earthq Spectra*. 2006; 22 (2): 367-390.
3. Somerville PG, Smith NF, Graves RW, Abrahamson NA. Modification of empirical strong ground motion attenuation relations to include the amplitude and duration effects of rupture directivity, *Seismol. Res. Lett.* 1997; 68(1): 199-222.
4. Mavroeidis GP, Papageorgiou AS. A mathematical representation of near-fault ground motions. *Bull Seismol Soc Am*. 2003; 93(3): 1099-1131.
5. Mollaioli F, Bosi A. Wavelet analysis for the characterization of forward-directivity pulse-like ground motion on energy-basis. Meccanica. 2012; 47(1): 203-219.
6. Amiri GG, Moghaddam SA. Extraction of forward-directivity velocity pulses using S-transform-based signal decomposition technique. *Bull Earthq Eng*. 2014; 12(4): 1583-1614.
7. Baker JW, Bozorgnia Y, Di Alessandro C, Chiou B, Erdik M, Somerville P, Silva W. GEM-PEER Global GMPEs project guidance for including near-fault effects in ground motion prediction models. *Proceedings of the 15th World Conference of Earthquake Engineering*, Lisbon, Portugal, 2012.

8. Chang Z, Sun X, Zhai C, Zhao J, Xie L. An empirical approach of accounting for the amplification effects induced by near-fault directivity. *Bull Earthq Eng.* 2018; 16(5): 1871-1885.

9. Dabaghi M, Kiureghian AD. Stochastic model for simulation of near-fault ground motions. *Earthq Eng Struct Dyn.* 2017; 46: 963-984.

10. Yang D, Zhou J. A stochastic model and synthesis for near-fault impulsive ground motions. *Earthq Eng Struct Dyn.* 2015; 44: 243-264.

11. Baker JW. Quantitative classification of near-fault ground motions using wavelet analysis. *Bull Seismol Soc Am.* 2007; 97(5): 1486-1501.

12. Zhai C, Chang Z, Li S, Chen Z, Xie L. Quantitative identification of near-fault pulse-like ground motions based on energy. *Bull Seismol Soc Am.* 2013; 103(5): 2591-2603.

13. Chang Z, Sun X, Zhai C, Zhao J, Xie L. An improved energy-based approach for selecting pulse-like ground motions. *Earthq Eng Struct Dyn.* 2016; 45(14): 2405-2411.

14. Guo G, Yang D, Liu Y. Duration effect of near-fault pulse-like ground motions and identification of most suitable duration measure. *Bull Earthq Eng.* 2018; 16 (11): 5095-5119.

15. Kohrangi M, Vamvatsikos D, Bazzurro P. Pulse-like versus non-pulse-like ground motion records: Spectral shape comparisons and record selection strategies. *Earthq Eng Struct Dyn.* 2018; 48(1): 46-64.

16. Nikfar F, Konstantinidis D. Peak sliding demands on unanchored equipment and contents in base-isolated buildings under pulse excitation. *J Struct Eng.* ASCE, 2017; 143(9): 04017086.

17. Mazza F. Seismic demand of base-isolated irregular structures subjected to pulse-type earthquakes. *Soil Dyn Earthq Eng.* 2018; 108:111-129.

18. Antonellis G, Panagiotou M. Seismic response of bridges with rocking foundations compared to fixed-base bridges at a near-fault site. *J Bridge Struct.* ASCE, 2014; 19(5): 04014007.

19. Ardakani SMS, Saiidi MS. Simple method to estimate residual displacement in concrete bridge columns under near-fault earthquake motions. *Eng Struct.* 2018; 176: 208-219.

20. Zou D, Han H, Liu J, Yang D, Kong X. Seismic failure analysis for a high concrete face rockfill dam subjected to near-fault pulse-like ground motions. *Soil Dyn Earthq Eng.* 2017; 98: 235-243.

21. Fang C, Zhong Q, Wang W, Hu S, Qiu C. Peak and residual responses of steel moment-resisting and braced frames under pulse-like near-fault earthquakes. *Eng Struct.* 2018; 177: 579-597.

22. Tian L, Yi S, Qu B. Orienting ground motion inputs to achieve maximum seismic displacement demands on electricity transmission towers in near-fault regions. *J Struct Eng.* ASCE, 2018; 144(4): 04018017.

23. Yi W-J, Zhou Y, Hwang H-J, Cheng Z-J, Hu X. Cyclic loading test for circular reinforced concrete columns subjected to near-fault ground motion. *Soil Dyn Earthq Eng.* 2018; 112: 8-17.

24. Bertero VV, Mahin SA, Herrera RA. Aseismic design implications of near-fault San Fernando earthquake records. *Earthq Eng Struct Dyn.* 1978; 6(1): 31-42.

25. Makris N, Black CJ. Evaluation of peak ground velocity as a "good" intensity measure for near-source ground motions. *J Struct Eng.* 2004; 130(9): 1032-1044.

26. Chang Z, De Luca F, Goda K. Automated classification of near-fault acceleration pulses using wavelet packets. *Comput-Aided Civ Infrastruct Eng.* 2019; (in press; DOI: 10.1111/mice.12437).

27. Ancheta TD, Darragh RB, Stewart JP, Seyhan E, Silva WJ, Chiou, BS-J, Wooddell KE, Graves RW, Kottke AR, Boore DM, Kishida T, Donahue JL. NGA-West2 database, *Earthq Spectra.* 2014; 30(3): 989-1005.

28. Goda K, Hong HP, Lee CS. Probabilistic characteristics of seismic ductility demand of SDOF systems with Bouc-Wen hysteretic behavior. *J Earthq Eng.* 2009; 13: 600-622.

29. Ruiz-Garcia J. Inelastic displacement ratios for seismic assessment of structures subjected to forward-directivity near-fault ground motions. *J Earthq Eng.* 2011; 15: 449-468.

30. Iervolino I, Chioccarelli E, Baltzopoulos G. Inelastic displacement ratio of near-source pulse-like ground motions. *Earthq Eng Struct Dyn.* 2012; 41: 2351-2357.

31. Dimakopoulou V, Fragiadakis M, Spyrakos C. Influence of modeling parameters on the response of degrading systems to near-field ground motions. *Eng Struct.* 2013; 53: 10-24.

32. Khoshnoudian F, Ahmadi E, Nik FA. Inelastic displacement ratios for soil-structure systems. *Eng Struct.* 2013; 57: 453-464.

33. Wen W-P, Zhai C-H, Li S, Chang Z, Xie L-L. Constant damage inelastic displacement ratios for the near-fault pulse-like ground motions. *Eng Struct.* 2014; 59: 599-607.

34. Durucan C, Dicleli M. A_p/V_p specific inelastic displacement ratio for seismic response estimation of structures. *Earthq Eng Struct Dyn.* 2015; 44: 1075-1097.

35. Yaghmaei-Sabegh S, Safari S, Ghayouri KA. Estimation of inelastic displacement ratio for base-isolated structures. *Earthq Eng Struct Dyn.* 2017; 47: 634-659.

36. Shahi SK, Baker JW. An efficient algorithm to identify strong-velocity pulses in multicomponent ground motions. *Bull Seismol Soc Am*. 2014; 104: 2456-2466.
37. Li C, Kunnath S, Zhai C. Influence of early-arriving pulse-like ground motions on ductility demands of single-degree-of-freedom systems. *J Earthq Eng*. 2019; (in press; DOI: 10.1080/13632469.2018.1466744).
38. Kalkan E, Kwong NS. Pros and cons of rotating ground motion records to fault-normal/parallel directions for response history analysis of buildings. *J Struct Eng,* ASCE, 2014; 140: 04013062.
39. Zeng YH, Chen CH. Fault rupture process of the 20 September 1999 Chi-Chi, Taiwan, earthquake. *Bull Seismol Soc Am*. 2001; 91(5): 1088-1098.
40. Wu C, Takeo M, Ide S. Source process of the Chi-Chi earthquake: a joint inversion of strong motion data and global positioning system data with a multifault model. *Bull Seismol Soc Am*. 2001; 91(5): 1128-1143.
41. Spudich P, Bayless JR, Baker JW, Chiou BSJ, Rowshandel B, Shahi SK, Somerville P. Final report of the NGA-West2 directivity working group. *PEER report*. 2013.
42. Bommer JJ, Martinez-Pereira A. The effective duration of earthquake strong motion. *J Earthq Eng.* 1999; 3(2): 127-172.
43. Alavi B, Krawinkler H. Behavior of moment-resisting frame structures subjected to near-fault ground motions. *Earthquake Eng. Struc. Dyn*. 2004; 33(6): 687-706.
44. Erduran E, Kunnath SK. Enhanced displacement coefficient method for degrading multi-degree-of-freedom systems. *Earthq Spectra*. 2010; 26(2): 311-326.
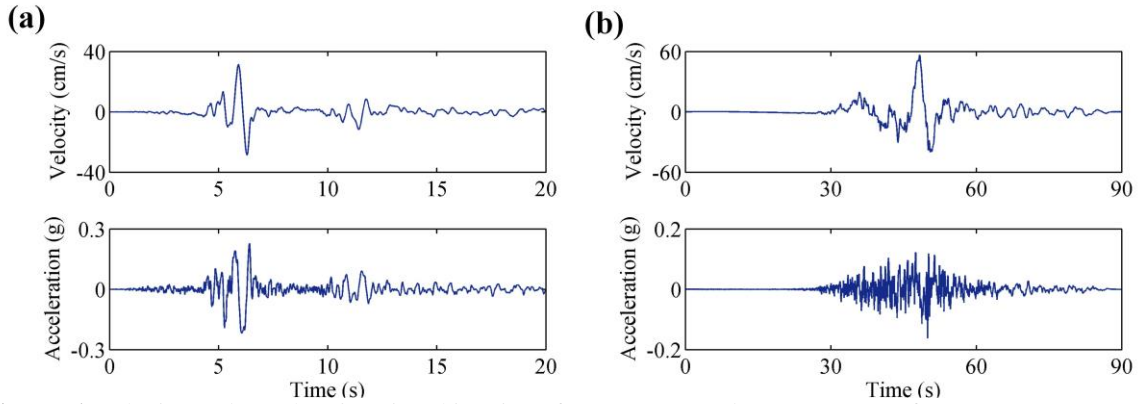
FIGURE 1 Velocity and acceleration time-histories of: (a) an *acc-pulse* component of A-OR2010 (RSN0645) recorded during the 1987 Whittier Narrows-01 earthquake; (b) a *non-acc-pulse* component of TCU040-E (RSN1483) recorded during the 1999 Chi-Chi earthquake. 'RSN' is the acronym for record sequence number according to the NGA West 2 database.
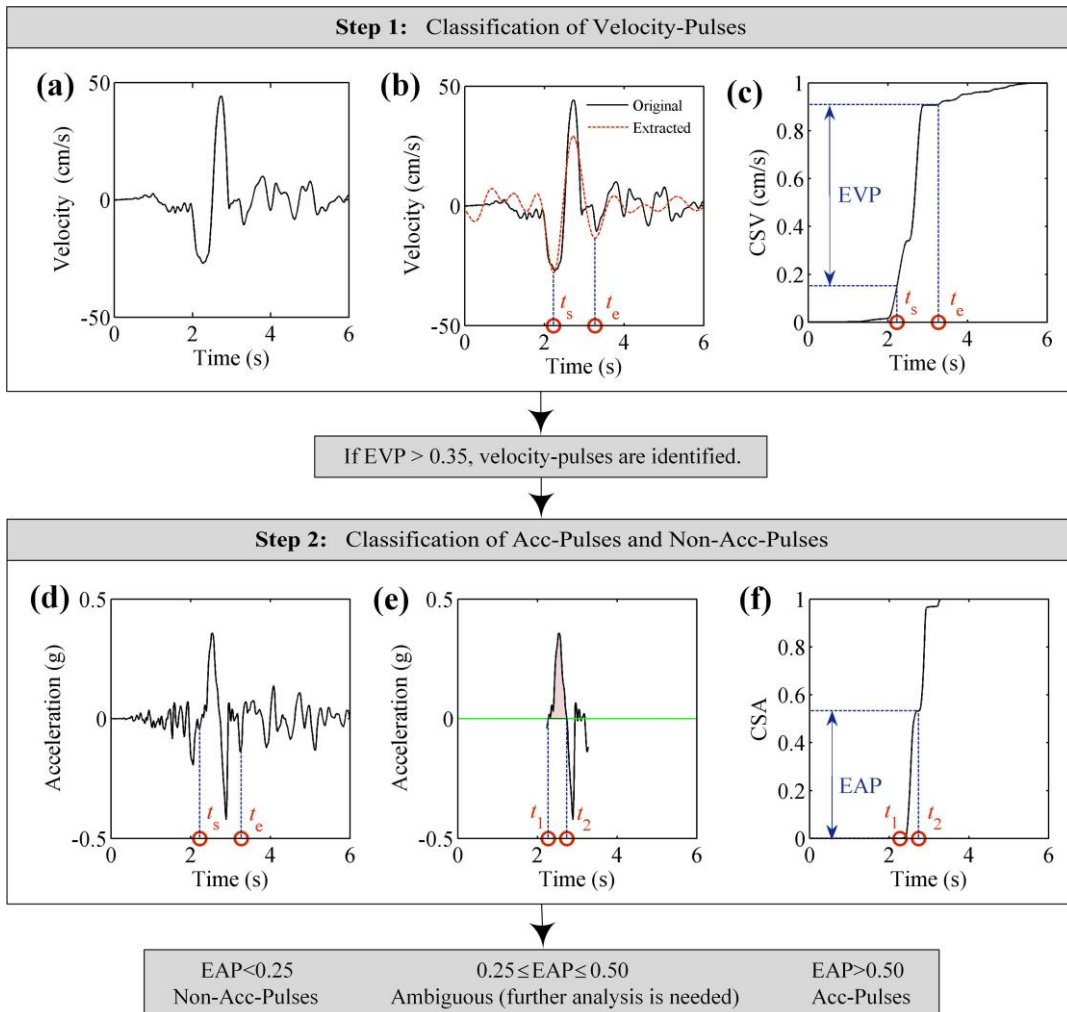
FIGURE 2 Flowchart of the automated algorithm for classifying *acc-pulses* and *non-acc-pulses*. This component of G06230 (RSN150) was recorded during the 1979 Goyote Lake earthquake.
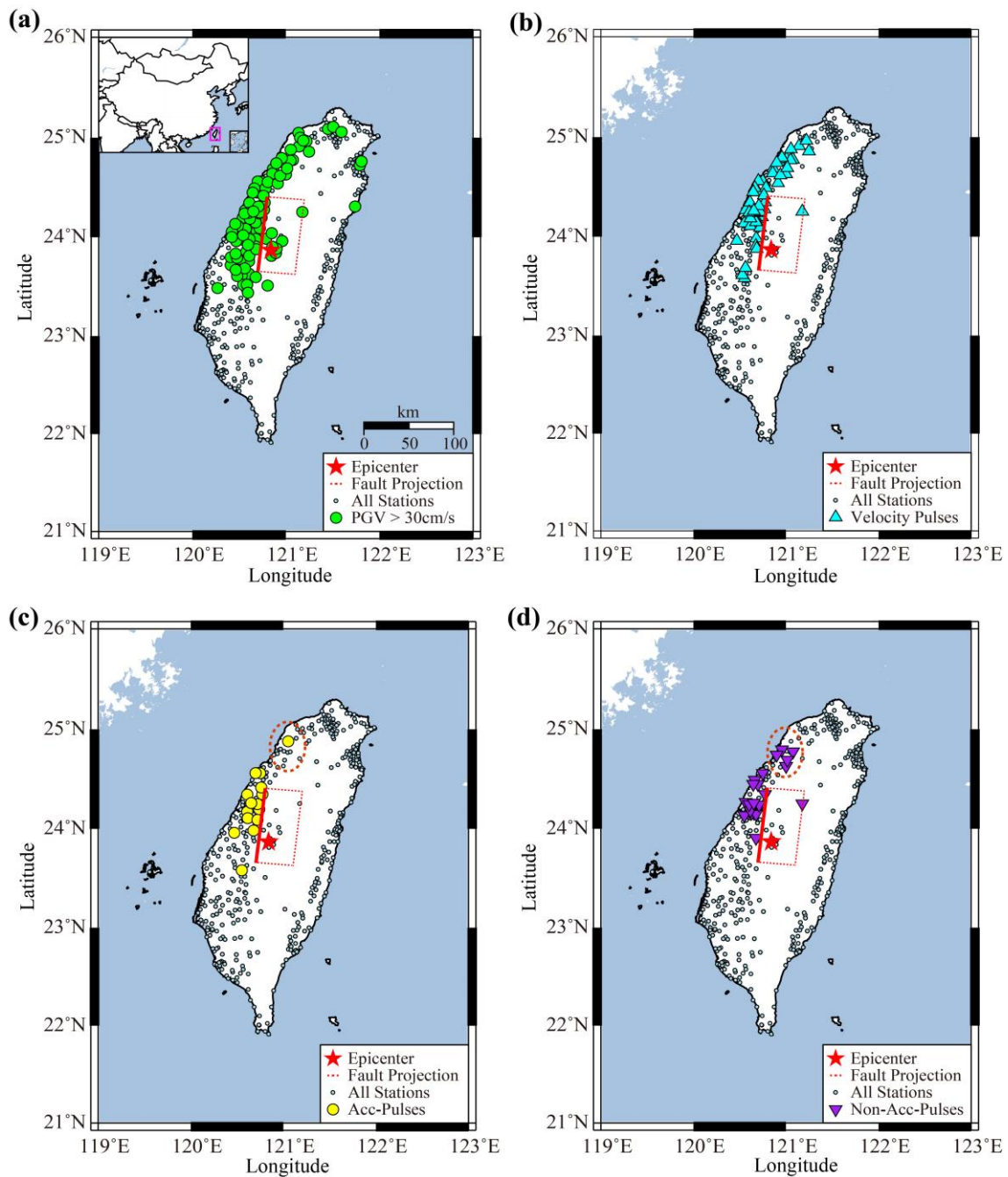
FIGURE 3 Map view of fault projection and observed ground motions from the 1999 Chi-Chi earthquake. The colored marks correspond to: (a) ground motions having PGV>30cm/s; (b) velocity-pulses; (c) *acc-pulses*; and (d) *non-acc-pulses*. Red dashed rectangle represents the fault plane projected onto the ground surface. The along-strike length is 96 km, and the along-dip width is 40 km. The strike angle of this event is at 5°, with the average dip and rake angles at 40° and 55°, respectively.
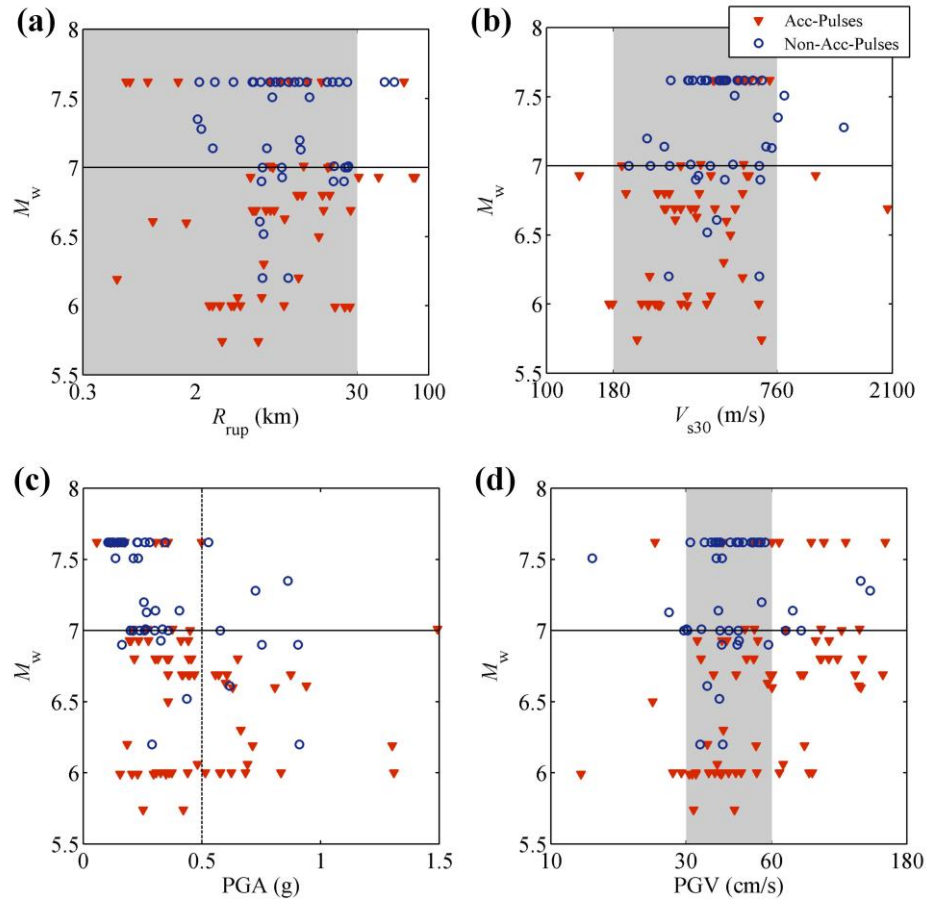
FIGURE 4 Distribution of ground motion parameters: (a) M_w versus R_{rup}; (b) M_w versus V_{s30}; (c) M_w versus PGA and (d) M_w versus PGV.
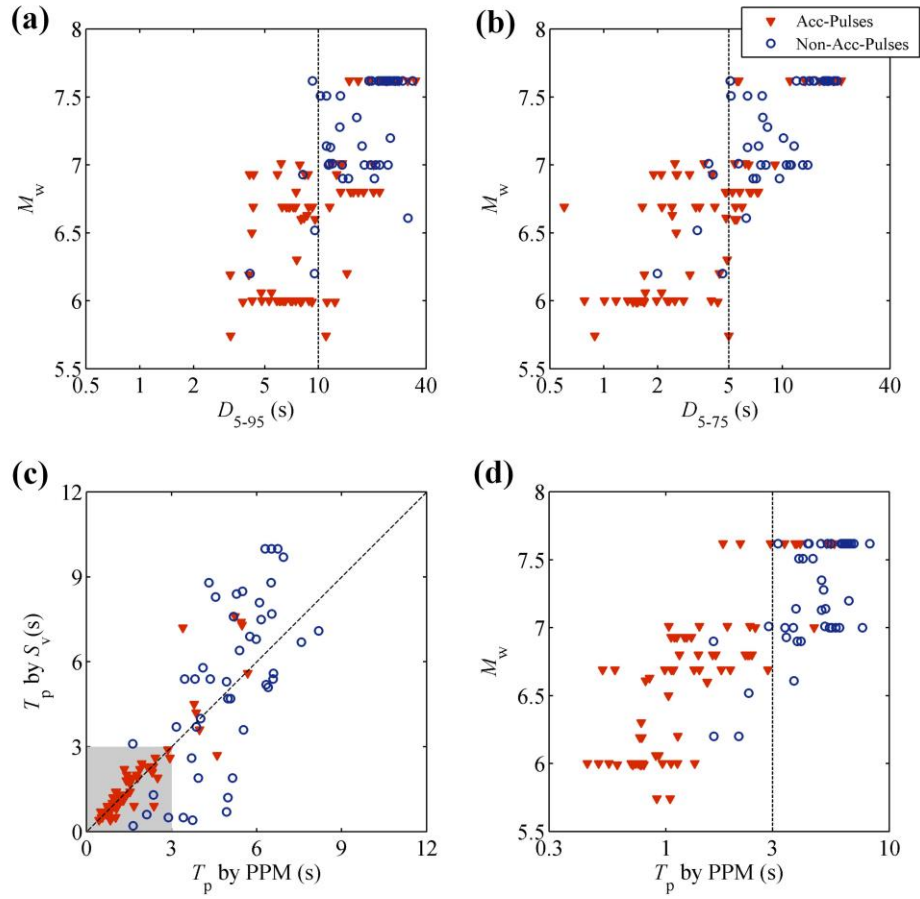
FIGURE 5 Characteristics of ground motion parameters: (a) M_w versus $D_{5\text{-}95}$; (b) M_w versus $D_{5\text{-}75}$; (c) T_p by PPM versus T_p by S_v; and (c) M_w versus T_p by PPM.
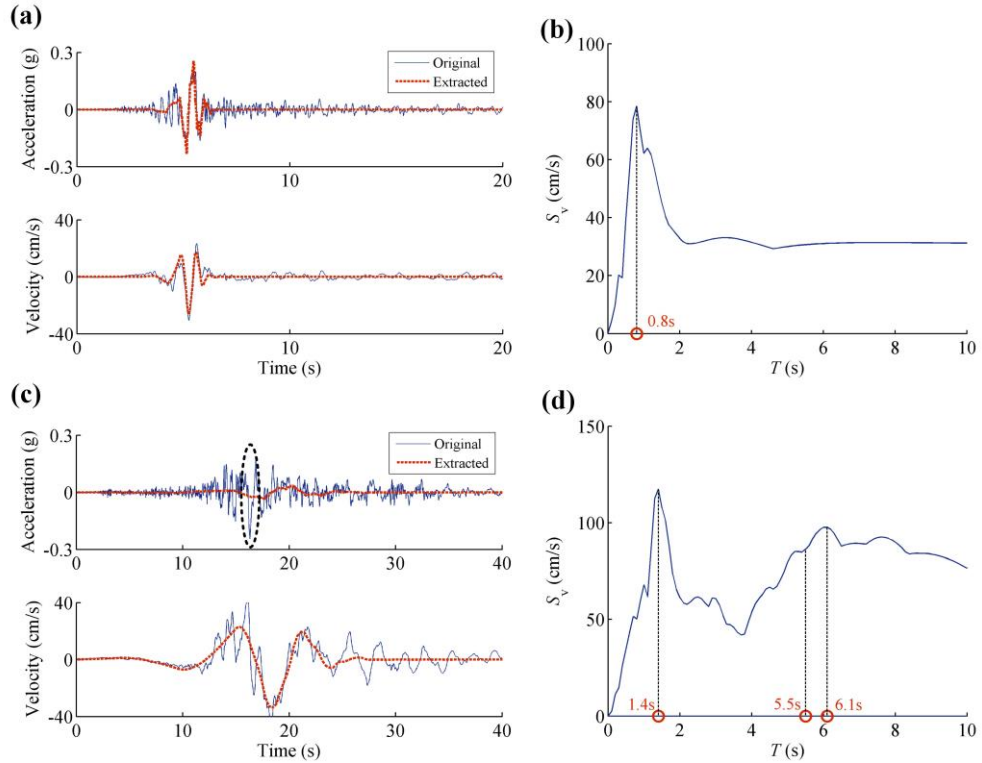
FIGURE 6 (a) Acceleration and velocity time-histories and (b) S_v of: A-DWN180 component recorded during the 1987 Whittier Narrows-01 earthquake (RSN0615); (c) acceleration and velocity time-histories and (d) S_v of: YER270 component recorded during the 1992 Lander earthquake (RSN0900). The top panel is for a typical *acc-pulse* while the bottom is for a *non-acc-pulse*. The dashed curves represent the pulse extracted using Baker's algorithm.
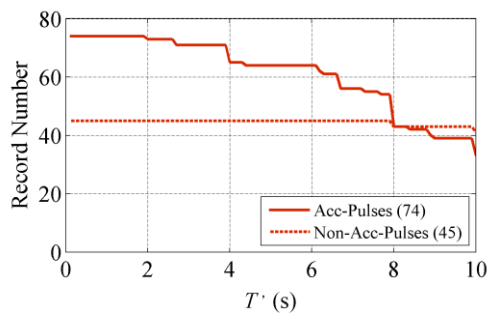
FIGURE 7 Record number of *acc-pulses* and *non-acc-pulses* versus usable spectral period T'.
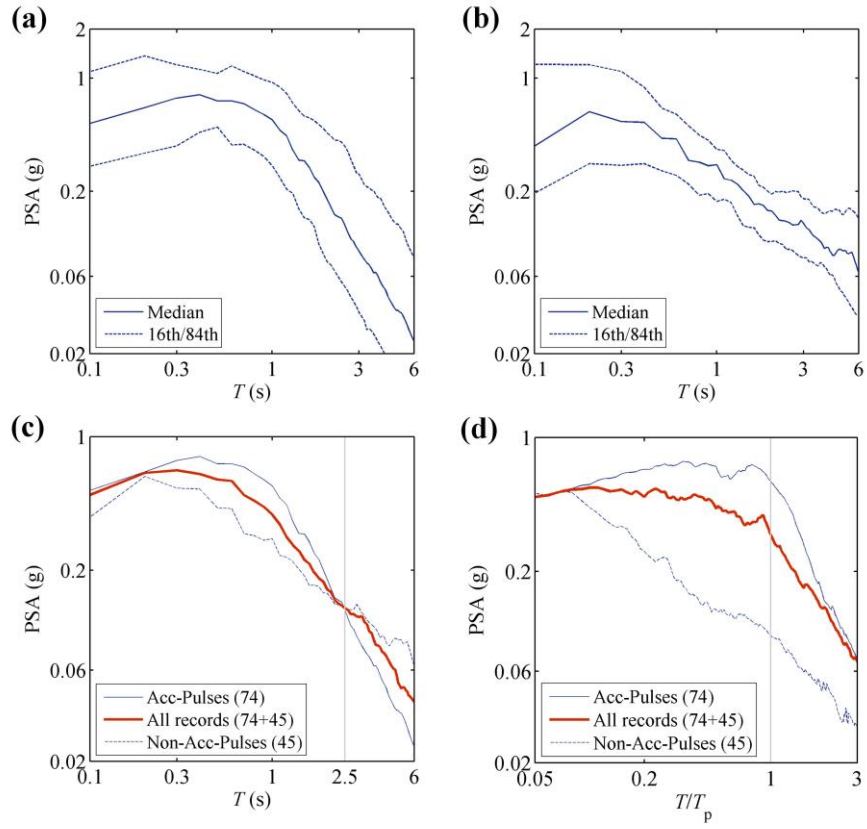
FIGURE 8 Median PSA of (a) *acc-pulses* and (b) *non-acc-pulses* as well as their 16th and 84th percentiles; (c) comparison of the median PSA values between *acc-pulses* and *non-acc-pulses*; (d) the same as subplot (c) but with T normalized by T_p.
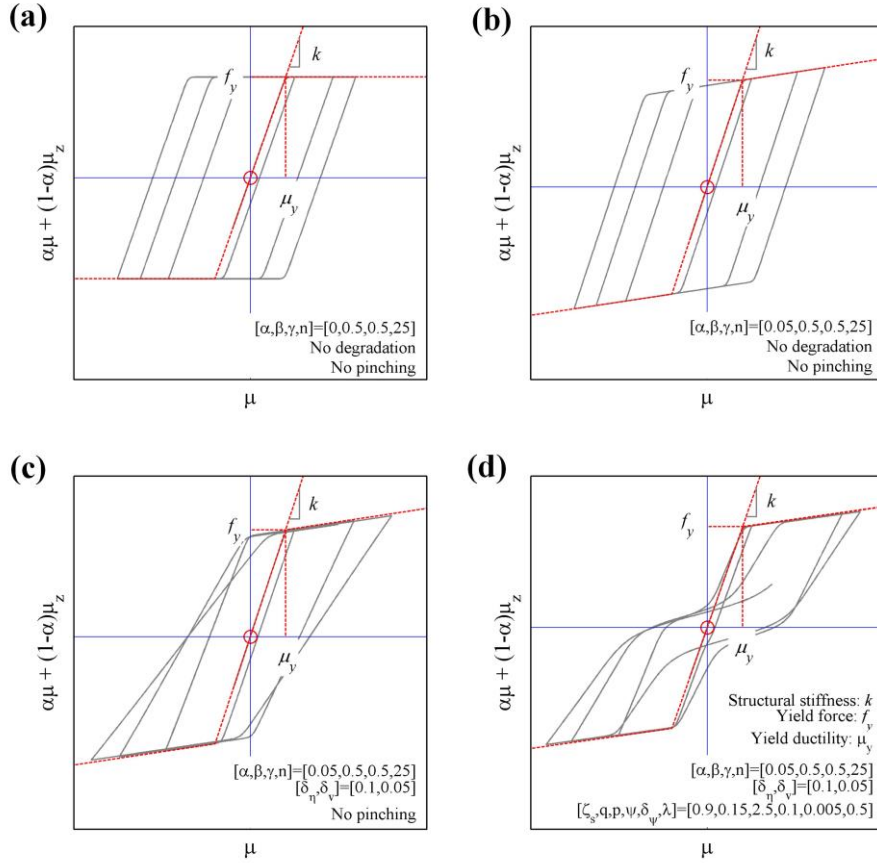
FIGURE 9 Illustration of the force-ductility relationship of the Bouc-Wen model subject to harmonic excitations with increasing amplitudes. (a) EPP system; (b) EPH system; (c) EPH-d system; (d) EPH-dp system.
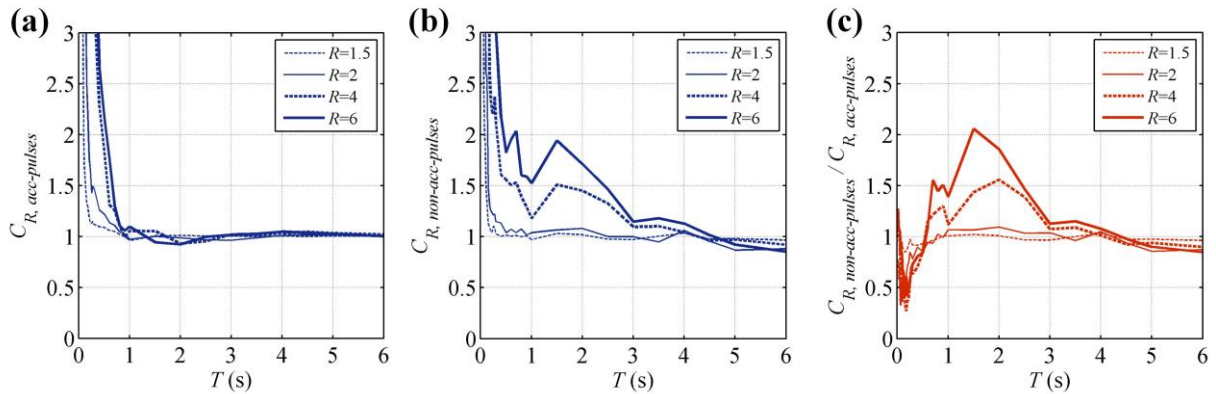
FIGURE 10 Median spectra for: (a) $C_{R, \, acc\text{-}pulses}$ and (b) $C_{R, \, non\text{-}acc\text{-}pulses}$; and (c) the spectral ratio of $C_{R, \, non\text{-}acc\text{-}pulses}$ / $C_{R, \, acc\text{-}pulses}$.
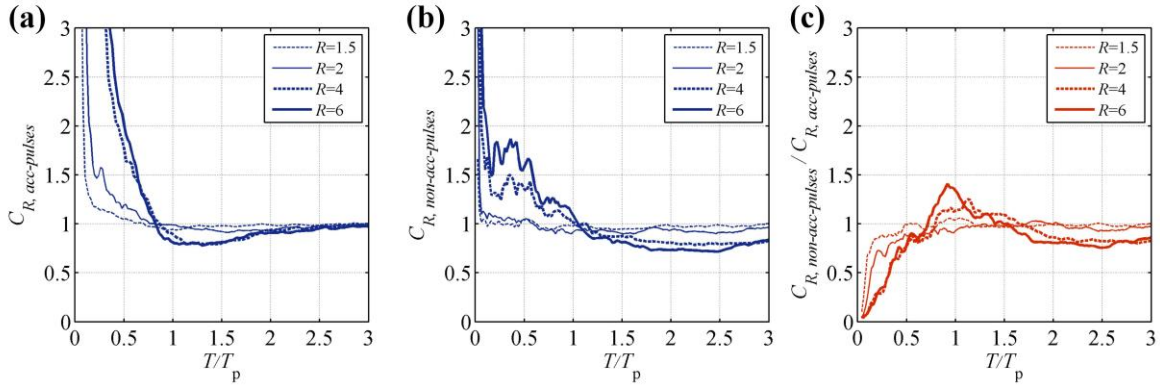
FIGURE 11 Illustration of T_p-normalized median spectra for: (a) $C_{R,\ acc\text{-}pulses}$; (b) $C_{R,\ non\text{-}acc\text{-}pulses}$; and (c) T_p-normalized median spectra for: $C_{R,\ non\text{-}acc\text{-}pulses}$ / $C_{R,\ acc\text{-}pulses}$.
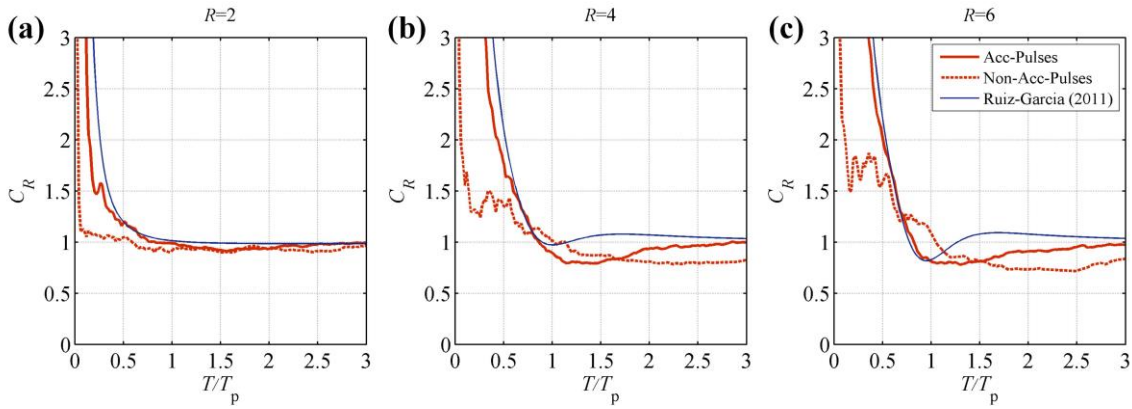
FIGURE 12 Comparisons of T_p-normalized median C_R spectra between *acc-pulses*, *non-acc-pulses* and the Ruiz-Garcia equation[28]. (a) R=2; (b) R=4; (c) R=6.
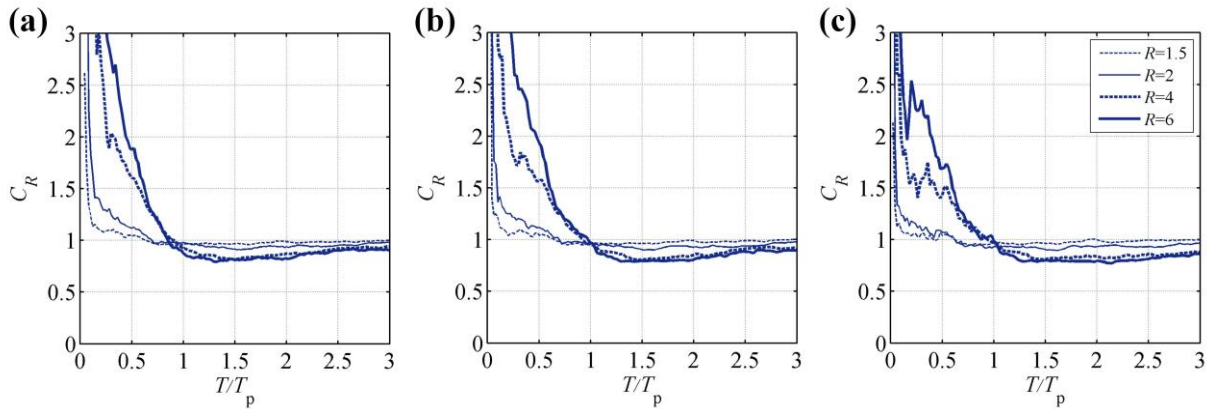
FIGURE 13 Local bumps produced as a result of mixing different proportions of *acc-pulses* and *non-acc-pulses*: (a) 74 *acc-pulses* plus 45 *non-acc-pulses*; (b) 45 *acc-pulses* plus 45 *non-acc-pulses*; (c) 20 *acc-pulses* plus 45 *non-acc-pulses*.
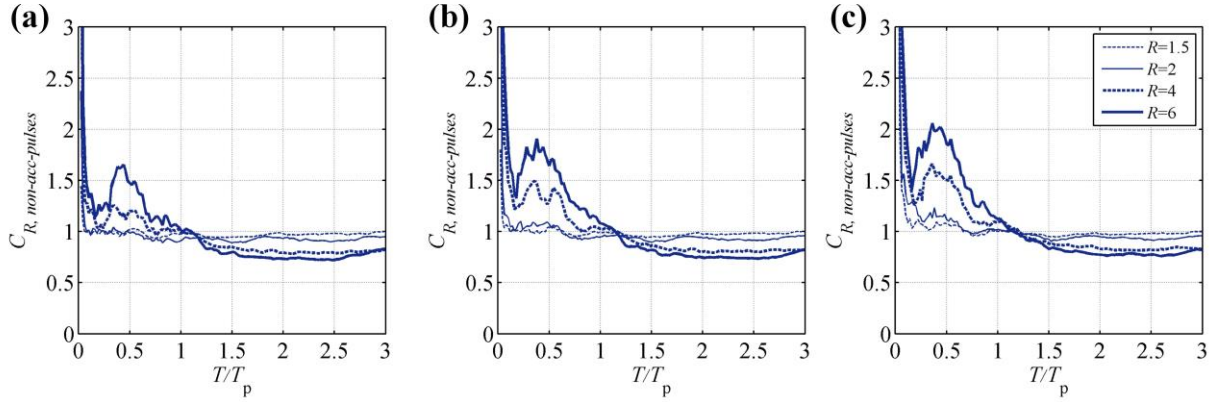
FIGURE 14 Local bumps in $C_{R,\ non\text{-}acc\text{-}pulses}$ for: (a) EPH systems; (b) EPH-d systems; and (c) EPH-dp systems. Recalling that the bumps in $C_{R,\ non\text{-}acc\text{-}pulses}$ for EPP systems have already been shown in Figure 11(b).
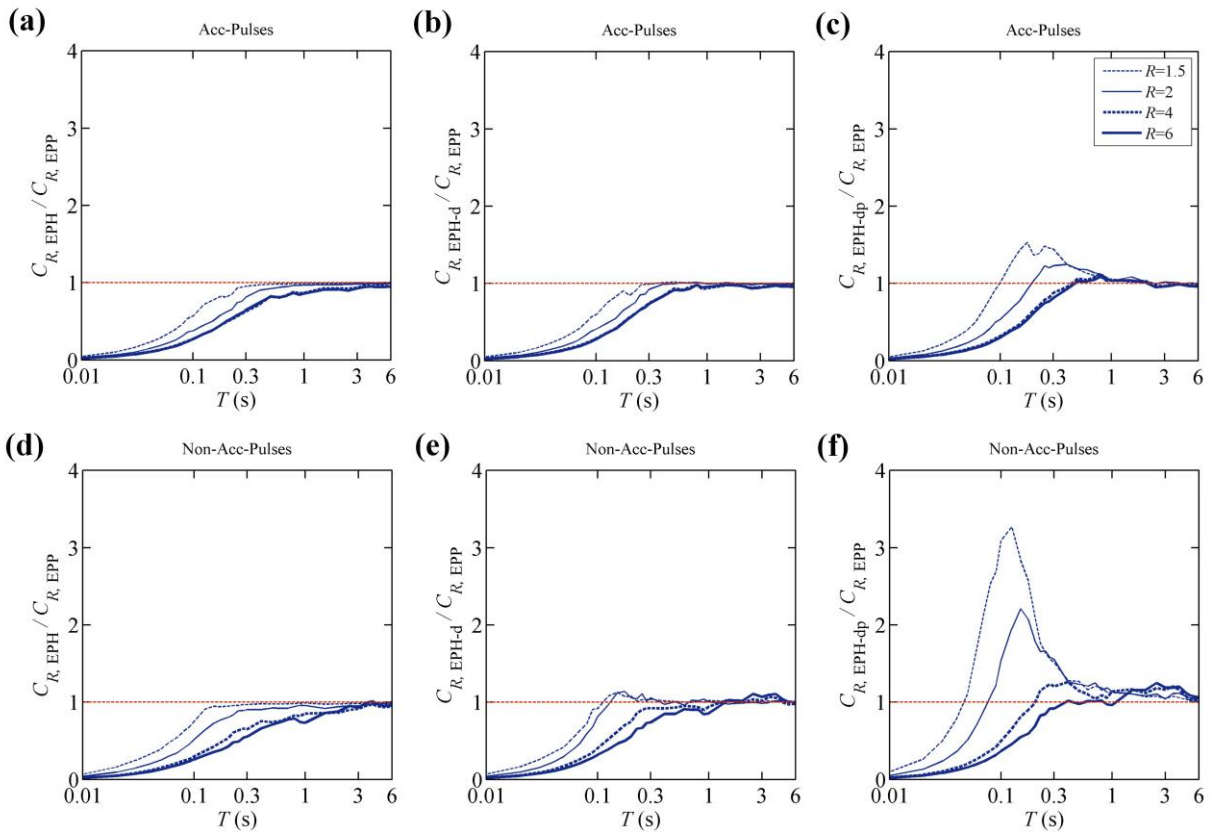
FIGURE 15 Effects of hysteretic models on the C_R spectra; top panels for *acc-pulses*: (a) $C_{R,\text{EPH}}/C_{R,\text{EPP}}$; (b) $C_{R,\text{EPH-d}}/C_{R,\text{EPP}}$; (c) $C_{R,\text{EPH-dp}}/C_{R,\text{EPP}}$; and bottom panels for *non-acc-pulses*: (d) $C_{R,\text{EPH}}/C_{R,\text{EPP}}$; (e) $C_{R,\text{EPH-d}}/C_{R,\text{EPP}}$; (f) $C_{R,\text{EPH-dp}}/C_{R,\text{EPP}}$.
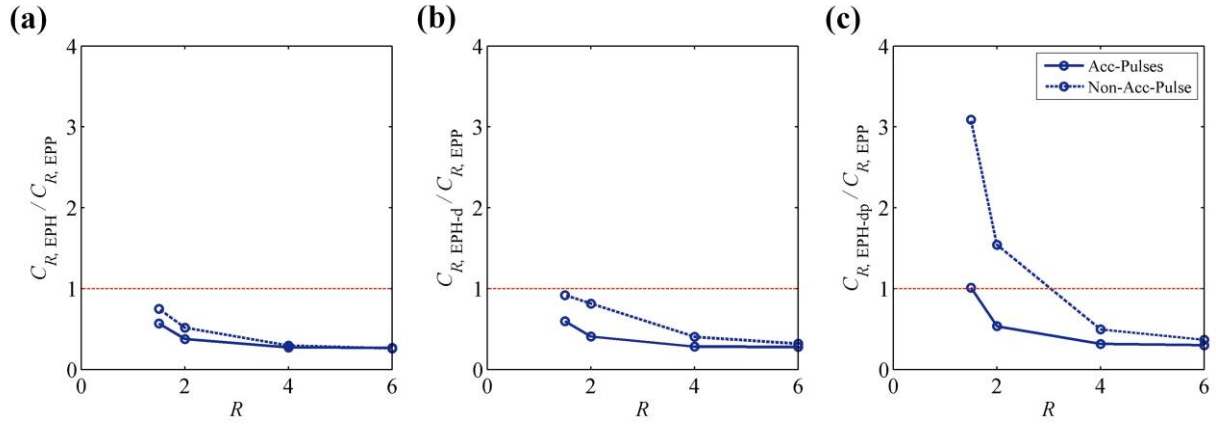
FIGURE 16 Ratios of C_R for: (a) EPH systems, (b) EPH-d systems and (c) EPH-dp systems to C_R for EPP systems as a function of R considering a short-period SDOF system with T=0.1s.

APPENDIX

TABLE A1   List of acc-pulse ground motions and relevant supporting information

RSN	Event	Compoent	M_w	R_{rup} (km)	V_{s30} (m/s)	PGA (g)	PGV (cm/s)	D_{5-95} (s)	D_{5-75} (s)	EVP	EAP	T_p (s) by S_v	T_p (s) by PPM
125	Friuli, Italy-01	TMZ000	6.5	15.8	505	0.36	22.8	4.2	2.5	0.448	0.598	1.0	0.5
149	Coyote Lake	G04360	5.74	5.7	222	0.25	31.9	11.0	5.0	0.380	0.581	0.9	1
150	Coyote Lake	G06230	5.74	3.1	663	0.42	44.4	3.2	0.9	0.743	0.533	1.0	0.9
451	Morgan Hill	CYC195	6.19	0.5	561	0.71	52.9	4.1	3.0	0.551	0.742	0.8	0.7
451	Morgan Hill	CYC285	6.19	0.5	561	1.30	78.5	3.2	1.7	0.551	0.701	0.8	0.8
529	N. Palm Springs	NPS210	6.06	4.0	345	0.69	66.0	4.8	2.1	0.602	0.533	0.9	1.2
540	N. Palm Springs	WWT180	6.06	6.0	425	0.48	38.5	5.5	1.7	0.395	0.635	0.9	0.5
614	Whittier, Narrows-01	A-BIR180	5.99	20.8	245	0.35	39.9	3.8	1.5	0.498	0.705	0.6	0.7
615	Whittier Narrows-01	A-DWN180	5.99	20.8	272	0.20	30.7	9.2	1.5	0.676	0.626	0.8	0.8
615	Whittier Narrows-01	A-DWN270	5.99	20.8	272	0.16	12.8	12.4	4.3	0.367	0.552	0.8	0.8
645	Whittier Narrows-01	A-OR2010	5.99	24.5	345	0.23	31.5	8.0	1.5	0.546	0.640	0.8	0.7
652	Whittier Narrows-01	A-DEL000	5.99	26.7	267	0.30	32.4	11.2	1.7	0.522	0.533	0.7	0.7
732	Loma Prieta	A02043	6.93	43.2	133	0.27	53.7	8.4	2.6	0.403	0.603	1.1	1.1
771	Loma Prieta	GGB270	6.93	79.8	584	0.23	40.1	5.9	2.6	0.521	0.681	1.2	1.3
787	Loma Prieta	SLC270	6.93	30.9	425	0.19	41.6	12.7	4.0	0.355	0.605	1.3	1.1
796	Loma Prieta	PRS090	6.93	77.4	594	0.20	32.8	8.7	3.0	0.478	0.673	1.1	1.4
825	Cape Mendocino	CPM000	7.01	7.0	568	1.49	122.6	6.2	2.5	0.665	0.605	2.4	0.9
953	Northridge-01	MUL009	6.69	17.2	356	0.44	59.3	9.3	6.0	0.425	0.519	1.1	0.9
983	Northridge-01	JGB022	6.69	5.4	526	0.57	76.2	6.9	4.2	0.590	0.503	2.9	2.9
1003	Northridge-01	STN020	6.69	27.0	309	0.47	37.5	11.6	5.5	0.368	0.529	0.6	0.6
1045	Northridge-01	WPI046	6.69	5.5	286	0.42	118.2	6.3	1.6	0.484	0.840	1.8	2
1045	Northridge-01	WPI316	6.69	5.5	286	0.36	59.2	8.8	2.1	0.477	0.763	1.4	2
1050	Northridge-01	PAC175	6.69	7.0	2016	0.42	45.0	4.3	0.6	0.504	0.552	0.5	0.5
1054	Northridge-01	PAR--L	6.69	7.5	326	0.56	76.1	6.6	2.4	0.460	0.511	1.0	1.2
1063	Northridge-01	RRS228	6.69	6.5	282	0.87	148.2	7.2	3.4	0.648	0.783	1.1	1.1
1085	Northridge-01	SCE281	6.69	5.2	371	0.45	60.4	7.4	3.4	0.454	0.613	1.3	2.2
1086	Northridge-01	SYL090	6.69	5.3	441	0.60	77.8	6.8	3.3	0.517	0.533	1.9	2.4
1182	Chi-Chi	CHY006-W	7.62	9.8	438	0.36	60.3	24.3	5.6	0.366	0.610	1.8	1.9
1473	Chi-Chi	TCU018-N	7.62	66.3	573	0.06	23.3	34.9	17.2	0.453	0.530	5.5	7.3
1492	Chi-Chi	TCU052-E	7.62	0.7	579	0.36	151.2	16.7	5.7	0.799	0.536	5.7	5.6
1501	Chi-Chi	TCU063-N	7.62	9.8	476	0.13	82.8	31.7	21.4	0.447	0.521	4.0	3.6
1502	Chi-Chi	TCU064-N	7.62	16.6	646	0.12	55.3	28.4	19.5	0.377	0.504	5.2	7.6
1504	Chi-Chi	TCU067-E	7.62	0.6	434	0.50	92.1	21.7	11.0	0.399	0.633	2.2	2.3
1510	Chi-Chi	TCU075-E	7.62	0.9	573	0.33	109.6	26.9	18.0	0.681	0.522	3.9	4.2
1519	Chi-Chi	TCU087-N	7.62	7.0	539	0.11	40.5	24.1	16.1	0.479	0.538	3.8	4.5
1529	Chi-Chi	TCU102-E	7.62	1.5	714	0.30	91.7	14.9	13.4	0.488	0.818	2.9	2.6
1548	Chi-Chi	TCU128-E	7.62	13.1	600	0.14	63.8	19.2	13.5	0.476	0.545	5.5	7.4
1550	Chi-Chi	TCU136-N	7.62	8.3	462	0.17	51.5	23.8	19.2	0.389	0.677	3.4	7.2
3548	Loma Prieta	LEX000	6.93	5.0	1070	0.44	85.8	4.3	2.1	0.600	0.538	1.1	1
3548	Loma Prieta	LEX090	6.93	5.0	1070	0.41	95.9	4.1	1.9	0.661	0.538	1.2	1.1
3744	Cape Mendocino	BNH360	7.01	12.2	566	0.21	48.3	13.4	3.6	0.594	0.517	1.9	2.2
3748	Cape Mendocino	FFS270	7.01	19.3	388	0.38	89.6	11.8	5.4	0.432	0.592	1.4	1.3
3748	Cape Mendocino	FFS360	7.01	19.3	388	0.27	52.2	13.6	6.2	0.426	0.548	1.0	1.4
3968	Tottori, Japan	TTRH02NS	6.61	1.0	310	0.94	122.2	8.3	4.8	0.428	0.555	0.8	0.8
4040	Bam, Iran	BAM-L	6.6	1.7	487	0.81	124.1	8.0	5.6	0.690	0.540	1.5	1.7
4040	Bam, Iran	BAM-T	6.6	1.7	487	0.63	60.2	9.6	5.4	0.651	0.516	1.5	1.4
4097	Parkfield-02, CA	SCN360	6	3.0	648	0.35	53.2	4.3	2.3	0.440	0.517	0.8	0.7
4098	Parkfield-02, CA	C01090	6	3.0	327	0.44	40.2	7.1	1.4	0.623	0.601	1.3	1.2
4098	Parkfield-02, CA	C01360	6	3.0	327	0.36	39.3	6.5	2.8	0.394	0.793	1.1	0.8
4100	Parkfield-02, CA	C02090	6	3.0	173	0.62	64.0	7.0	1.0	0.537	0.516	0.7	0.9
4100	Parkfield-02, CA	C02360	6	3.0	173	0.37	44.8	6.1	2.3	0.470	0.547	0.8	0.7
4102	Parkfield-02, CA	C03090	6	3.6	231	0.33	28.9	6.4	1.6	0.478	0.709	0.7	0.6
4102	Parkfield-02, CA	C03360	6	3.6	231	0.58	37.8	6.5	1.6	0.538	0.771	0.8	0.9
4103	Parkfield-02, CA	C04090	6	4.2	410	0.58	32.3	5.3	1.7	0.485	0.724	0.6	0.5
4103	Parkfield-02, CA	C04360	6	4.2	410	0.51	26.9	4.8	1.5	0.478	0.849	0.5	0.7
4107	Parkfield-02, CA	COW360	6	2.5	178	0.83	81.4	7.5	1.5	0.634	0.602	1.0	0.9
4115	Parkfield-02, CA	PRK360	6	2.7	265	0.31	46.9	8.8	4.0	0.651	0.593	1.1	1.2
4116	Parkfield-02, CA	Z14090	6	8.8	246	1.31	83.6	5.9	2.0	0.364	0.730	0.7	0.6
4116	Parkfield-02, CA	Z14360	6	8.8	246	0.58	42.3	7.1	2.5	0.402	0.559	0.7	0.7
4126	Parkfield-02, CA	SC1090	6	3.8	261	0.68	36.0	6.1	0.8	0.664	0.540	0.8	0.8
4126	Parkfield-02, CA	SC1360	6	3.8	261	0.83	39.9	8.1	1.2	0.547	0.631	0.4	0.4
4228	Niigata, Japan	NIGH11EW	6.63	8.9	375	0.60	58.1	8.6	2.4	0.467	0.654	0.8	0.4
4480	L'Aquila, Italy	GX066XTE	6.3	6.3	475	0.66	40.5	7.6	4.9	0.488	0.599	0.8	0.6
4847	Chuetsu-oki	65010EW	6.8	11.9	383	0.46	89.2	15.7	4.8	0.424	0.686	1.4	1.8
4847	Chuetsu-oki	65010NS	6.8	11.9	383	0.30	49.0	20.3	7.4	0.422	0.543	2.3	2.1
4850	Chuetsu-oki	65013NS	6.8	16.9	562	0.31	52.0	15.1	5.3	0.375	0.601	1.7	0.9
4856	Chuetsu-oki	65025EW	6.8	11.1	294	0.65	95.6	7.5	4.9	0.492	0.639	2.3	2.2
4875	Chuetsu-oki	65058EW	6.8	12.0	283	0.36	102.6	22.0	5.8	0.400	0.639	2.4	2.6
4879	Chuetsu-oki	65084EW	6.8	19.0	266	0.21	33.8	17.9	6.6	0.363	0.644	1.2	1.2

4896	Chuetsu-oki	SG01EW	6.8	11.0	201	0.44	125.3	13.3	6.7	0.414	0.516	2.4	2.3
4896	Chuetsu-oki	SG01NS	6.8	11.0	201	0.35	90.0	16.7	7.2	0.395	0.555	1.6	1.9
6889	Darfield, New Zealand	CHHCN01W	7	18.4	194	0.21	67.2	20.4	9.1	0.389	0.583	4.6	2.7
6911	Darfield, New Zealand	HORCN18E	7	7.3	326	0.45	106.0	7.9	6.5	0.436	0.533	2.5	1.9
8134	Christchurch, New Zealand	SMTCN88W	6.2	11.3	248	0.18	35.6	14.5	4.4	0.368	0.603	1.1	1

TABLE A2 List of non-acc-pulse ground motions and relevant supporting information

RSN	Event	Compoent	M_w	R_{rup} (km)	V_{s30} (m/s)	PGA (g)	PGV (cm/s)	D_{5-95} (s)	D_{5-75} (s)	EVP	EAP	T_p (s) by S_v	T_p (s) by PPM
143	Tabas, Iran	TAB-T1	7.35	2.1	767	0.86	123.6	16.3	7.8	0.663	0.104	5.0	4.7
802	Loma Prieta	STG090	6.93	8.5	381	0.33	46.0	8.2	4.1	0.663	0.176	3.5	5.4
879	Landers	LCN260	7.28	2.2	1369	0.73	133.6	13.1	8.2	0.746	0.143	5.1	4.7
1148	Kocaeli, Turkey	ARE000	7.51	13.5	523	0.21	14.0	11.1	7.7	0.482	0.109	4.6	8.3
1148	Kocaeli, Turkey	ARE090	7.51	13.5	523	0.13	40.1	10.2	5.1	0.611	0.174	4.1	5.8
1165	Kocaeli, Turkey	IZT090	7.51	7.2	811	0.23	38.3	13.3	6.4	0.640	0.243	3.9	1.9
1475	Chi-Chi	TCU026-E	7.62	56.1	570	0.12	37.9	24.7	12.0	0.583	0.219	6.8	10
1480	Chi-Chi	TCU036-N	7.62	19.8	478	0.12	47.5	27.0	15.1	0.437	0.241	6.3	5.2
1481	Chi-Chi	TCU038-N	7.62	25.4	298	0.14	38.8	25.2	13.1	0.459	0.118	6.5	7.7
1483	Chi-Chi	TCU040-E	7.62	22.1	362	0.16	56.8	24.8	14.1	0.563	0.200	4.9	5.3
1489	Chi-Chi	TCU049-E	7.62	3.8	487	0.28	53.6	21.6	17.7	0.587	0.160	6.3	10
1490	Chi-Chi	TCU050-E	7.62	9.5	542	0.15	36.7	26.3	17.6	0.482	0.157	6.5	10
1491	Chi-Chi	TCU051-E	7.62	7.6	350	0.16	53.9	24.3	17.4	0.519	0.161	5.5	8.5
1493	Chi-Chi	TCU053-E	7.62	6.0	455	0.23	39.6	22.3	17.1	0.419	0.190	4.3	8.8
1494	Chi-Chi	TCU054-E	7.62	5.3	461	0.15	46.0	23.9	17.1	0.530	0.195	6.1	8.1
1496	Chi-Chi	TCU056-E	7.62	10.5	403	0.16	42.9	26.2	20.2	0.476	0.119	6.5	8.8
1511	Chi-Chi	TCU076-E	7.62	2.7	615	0.34	51.9	29.5	17.5	0.433	0.242	3.2	3.7
1515	Chi-Chi	TCU082-E	7.62	5.2	473	0.23	54.9	23.1	17.9	0.563	0.222	6.2	7.5
1519	Chi-Chi	TCU087-E	7.62	7.0	539	0.12	45.0	23.9	14.9	0.405	0.179	5.3	8.4
1520	Chi-Chi	TCU088-N	7.62	18.2	665	0.53	34.8	9.2	5.1	0.436	0.050	4.9	0.7
1526	Chi-Chi	TCU098-E	7.62	47.7	347	0.11	45.7	33.6	19.4	0.519	0.179	8.2	7.1
1527	Chi-Chi	TCU100-E	7.62	11.4	535	0.11	38.0	26.4	18.2	0.368	0.151	6.4	5.1
1528	Chi-Chi	TCU101-N	7.62	2.1	389	0.26	51.0	19.2	17.0	0.386	0.170	4.4	5.4
1531	Chi-Chi	TCU104-E	7.62	12.9	410	0.10	31.0	27.8	19.5	0.393	0.202	6.6	5.4
1550	Chi-Chi	TCU136-W	7.62	8.3	462	0.17	45.4	19.8	17.5	0.569	0.249	6.9	9.7
1605	Duzce, Turkey	DZC180	7.14	6.6	282	0.40	71.2	11.1	7.3	0.364	0.249	3.8	5.4
1787	Hector Mine	HEC000	7.13	11.7	726	0.27	26.0	11.7	6.4	0.472	0.183	5.0	1.2
3749	Cape Mendocino	FFT270	7.01	20.4	355	0.33	33.9	11.5	3.9	0.444	0.210	2.9	0.5
3750	Cape Mendocino	LFS360	7.01	25.9	516	0.26	30.1	12.0	5.7	0.480	0.169	5.1	1.9
3947	Tottori, Japan	SMNH01EW	6.61	5.9	446	0.62	35.5	31.6	6.3	0.549	0.162	3.7	0.4
4031	San Simeon, CA	36695090	6.52	6.2	411	0.44	39.3	9.6	3.3	0.391	0.230	2.4	1.3
5658	Iwate	IWTH26NS	6.9	6.0	371	0.90	58.4	14.7	6.8	0.377	0.157	1.6	3.1
5663	Iwate	MYG004NS	6.9	20.2	479	0.75	45.4	13.7	7.1	0.418	0.096	3.9	3.7
5810	Iwate	56362EW	6.9	24.1	655	0.16	40.0	20.6	9.6	0.389	0.235	4.0	4
6897	Darfield, New Zealand	DSLCN27W	7	8.5	296	0.26	39.4	18.1	10.5	0.567	0.078	6.0	6.8
6897	Darfield, New Zealand	DSLCN63E	7	8.5	296	0.24	67.3	19.6	13.0	0.448	0.148	5.4	6.4
6915	Darfield, New Zealand	HVSCS26W	7	24.5	422	0.58	42.4	13.6	8.1	0.456	0.190	3.4	0.5
6928	Darfield, New Zealand	LPCCS10E	7	25.7	650	0.36	30.3	11.4	7.6	0.570	0.109	5.5	3.6
6953	Darfield, New Zealand	PRPCW	7	24.6	206	0.20	29.4	22.0	11.2	0.354	0.235	3.7	2.6
6975	Darfield, New Zealand	TPLCN27W	7	6.1	249	0.30	76.3	24.5	13.9	0.382	0.150	7.6	6.7
6975	Darfield, New Zealand	TPLCS63W	7	6.1	249	0.21	45.8	20.9	11.0	0.462	0.136	5.8	6.9
8124	Christchurch, New Zealand	RHSCN86W	6.2	9.4	293	0.29	33.5	9.5	4.6	0.406	0.244	2.1	0.6
8158	Christchurch, New Zealand	LPCCN10W	6.2	6.1	650	0.91	40.3	4.1	2.0	0.545	0.184	1.6	0.2
8164	Duzce, Turkey	487-NS	7.14	2.7	690	0.30	38.9	17.6	11.6	0.395	0.102	5.2	7.6
8606	El Mayor-Cucapah	CIWESHNN	7.2	11.4	242	0.26	55.3	25.3	10.1	0.473	0.129	6.6	5.6